IEEE Photonics Journal
An IEEE Photonics Society Publication

Open Access

SVM-Assisted Realization and Demonstration of Indoor 4 Mb/s Non-Line-of-Sight Visible Light Communication With Second-Order Reflection

Volume 11, Number 5, October 2019

Yonghe Zhu
Chen Gong
Jianghua Luo
Zhengyuan Xu
Weiqiang Xu

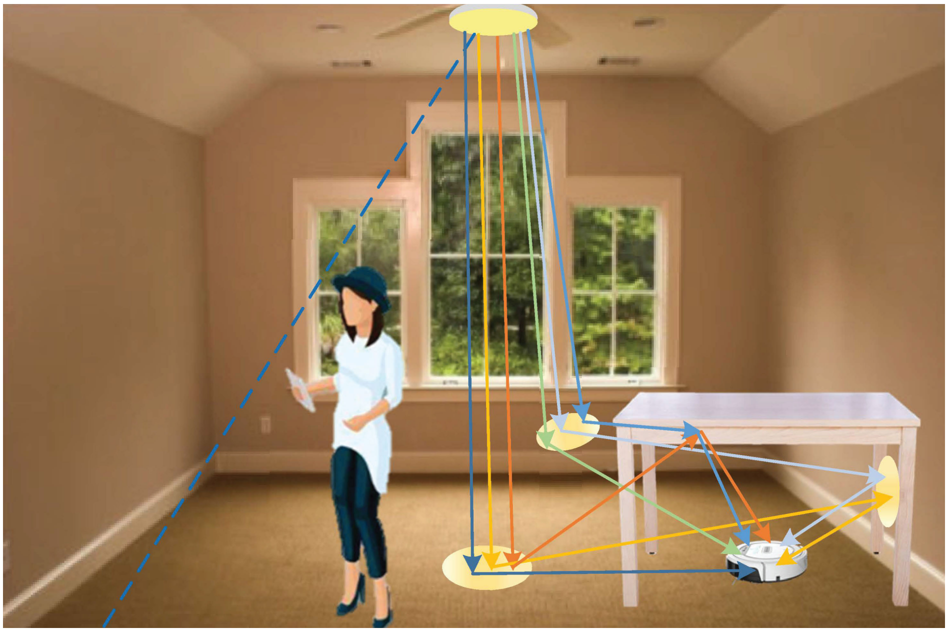

DOI: 10.1109/JPHOT.2019.2938178

SVM-Assisted Realization and Demonstration of Indoor 4 Mb/s Non-Line-of-Sight Visible Light Communication With Second-Order Reflection

Yonghe Zhu,[1] **Chen Gong**,[1] **Jianghua Luo,**[2,3] **Zhengyuan Xu**,[1]
and Weiqiang Xu[4]

[1]Key Laboratory of Wireless-Optical Communications, Chinese Academy of Sciences,
School of Information Science and Technology, University of Science and Technology of
China, Hefei 230027, China
[2]National Mobile Communications Research Laboratory, Southeast University, Nanjing
210096, China
[3]Zhongshan Zhongchuang Technology Research Institute of Opto-electronics Industry,
Zhongshan 528415, China
[4]School of Information Science and Technology, Zhejiang Sci-Tech University, Hangzhou
310018, China

DOI:10.1109/JPHOT.2019.2938178

Manuscript received July 29, 2019; revised August 22, 2019; accepted August 26, 2019. Date of publication August 29, 2019; date of current version September 10, 2019. This work was supported in part by the National Key Research and Development Program of China under Grant 2018YFB1801904, in part by the Key Program of National Natural Science Foundation of China under Grant 61631018, in part by the Key Research Program of Frontier Sciences of CAS under Grant QYZDY-SSW-JSC003, and in part by the Open Research Fund of National Mobile Communications Research Laboratory, Southeast University, under Grant 2019D14. Corresponding author: Chen Gong (e-mail: cgong821@ustc.edu.cn).

Abstract: Non-line of sight (NLOS) visible light communication (VLC) from reflections can expand the application of VLC beyond the line-of-sight (LOS) link. We demonstrate the experimental results on such indoor NLOS VLC, up to the second-order reflection. The avalanche photodiode (APD) receiver is employed due to the strong ambient light background. Manchester coding is adopted at the transmitter, and digital filtering is adopted at the receiver. We propose an Support Vector Machine (SVM) detection method to solve the significant distortion issue due to weak signal of the NLOS link. Experimental results on the second-order reflection-based VLC demonstrate that the detection error probability of the proposed SVM detection can be reduced up to at least two orders of magnitude compared with the Gaussian approximation-based detection, and can reach 10^{-4} at bit rate 4 Mbps. Thus, low-data rate applications can be achieved by VLC with only the second-order reflection, which implies the potential in speech/image/control message transmission and Internet of Things (IoT) applications, for example the mobile robots that may operate in the shadow or even under a table. Experimental results on the second-order reflection at different transmission rates and different sampling rates are also demonstrated.

Index Terms: NLOS VLC, second-order reflection, SVM detection, Manchester coding, IoT.

1. Introduction

As the number of mobile devices and users is increasing significantly, the demand for high transmission bandwidth is emerging. Visible light communication (VLC) is attracting more and more research interest due to its potential high transmission bandwidth, high transmission rate, data security, and no electromagnetic interference [1]–[5]. Currently, a variety of VLC transmission approaches have been proposed to increase the communication capability [6]–[10]. As an important supplement to radio frequency (RF) communication [11], [12], VLC is considered to be one of the most important green information technologies [13].

As the light wave has poor penetrating capability due to much shorter wavelength in case of an obstacle between the receiver and the transmitter, non-line of sight (NLOS) channels with only reflections should be explored. The NLOS channel can expand the application range of VLC, especially for industrial Internet-of-Things (IoT) application scenarios with electromagnetic radiation restriction. It has been shown that the NLOS channels can be non-negligible for VLC systems [14], where the corresponding channel impulse response (CIR) exhibits continuous waveform [15].

In order to prove the feasibility of indoor NLOS VLC, the CIR calculation has been proposed in [14]. In this method, an cuboid room with Lambertian reflectors is considered, whose inner surface is divided into many small reflection micro-elements and an accurate CIR can be obtained by integrating the individual micro-elements with high computational complexity. To reduce the computational complexity, a more efficient method has been proposed [15], where the NLOS channel is decomposed into a number of components with different propagation categories. Such method can offer sufficiently accurate results with low computational complexity.

Existing works on the demonstration of NLOS VLC include the mobile phone camera based VLC [16], which can achieve 5 Kbps at a transmission distance 100 cm. A data rate of 100 bps can be achieved at distance 300 m with BER below 6.1×10^{-5} without pointing requirement [17], which validated the feasibility of the NLOS VLC using camera as the receiver. Work [18] explores the performance of NLOS visible light communication system based on channel simulations for Sub-Carrier Pulse Position Modulation (SC-LPPM), which explores the effect of different VLC systems and environmental parameters on the BER performance for LOS/NLOS SC-LPPM scenarios.

Against the above background, there still exists a fundamental question, whether NLOS indoor visible light communication can be realized via experiments at symbol rate up to the order of Mega bits per second with BER below 10^{-3}, especially under the second-order reflection from the wall, floor and ceiling. The rationale of selecting 10^{-3} as the BER threshold is that it is the typical threshold for speech communication and can be readily corrected by a standard error correcting code. The potential applications include mobile robots that may operate in the shadow or even under a table. In this work, we confirm this via demonstrating the feasibility of indoor NLOS VLC from the wall, floor and ceiling reflections, up to the second order using avalanche photodiode (APD) as the receiver. In contrast to the photomultiplier tube (PMT) receiver used in [19], [20] for VLC under weak ambient light. In this work, we adopt APD to improve the signal-to-noise ratio (SNR) due to the strong ambient light. In addition, we propose a support vector machine (SVM) detection method for NLOS indoor VLC and compare its performance with the Gaussian approximation-based detection. We demonstrate the experimental results on the second-order reflection-based VLC, where the detection error probability of proposed SVM detection can be reduced at least two orders of magnitudes compared with Gaussian approximation-based detection, and reach 10^{-4} at bit rate 4 Mbps, which can be readily further corrected by a standard error correcting code. Such results demonstrate the feasibility of a reliable NLOS VLC link for low-data rate applications without line-of-sight (LOS) links, for example speech/image/control message/low-resolution video transmission and Internet of Things (IoT) applications, where the position and receiving angle of the receiver can be more flexible to improve the communication mobility.

The remainder of this paper is organized as follows. We investigative the indoor NLOS VLC system modeling in Section 2. We describe the signal processing adopted in the indoor NLOS VLC in Section 3. We present experimental results on the NLOS VLC in Secion 4. We conclude this work in Section 5.

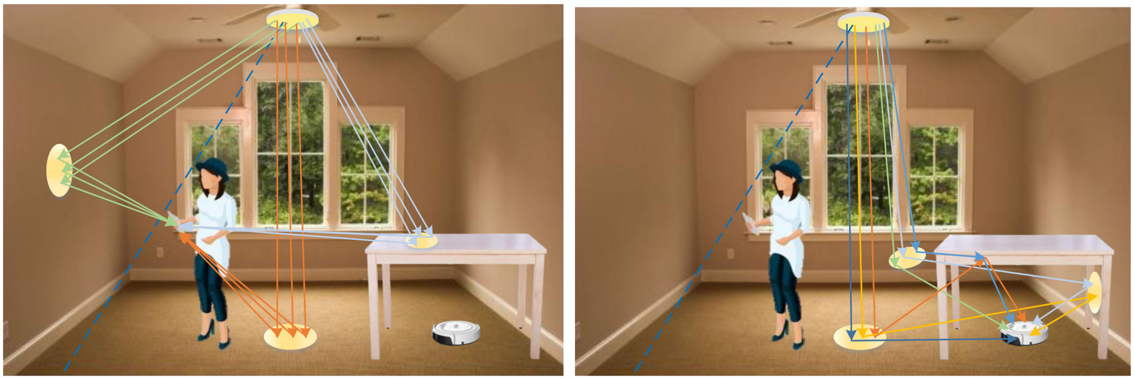

(a) (b)

Fig. 1. Examples on the NLOS VLC link. (a) The first-order reflection from the LED to the hand-held terminal. (b) The second-order reflection from the LED to the robot under the table.

2. System Modeling

The indoor NLOS reflection-based VLC system under consideration consists of a white LED transmitter, the NLOS channels with the wall, table and floor reflections, and a receiver based on APD. The channel path loss is determined by the room size, the reflection coefficients of the ceiling, walls and other objects, the positions and orientations of the transmitter and receiver, as well as the location and size of the window. The received optical power can be expressed as:

$$P_{r-nlos} = H_{nlos}(0)P_t = \sum_{i=1}^{\infty} H_i(0)P_t, \tag{1}$$

where $H_i(0)$ represents the direct-current (DC) gain of light undergoing exactly i reflections, P_{r-nlos} and P_t represent the transmission power and receiving power, respectively.

Consider the communication scenarios shown in Fig. 1. The receiver can receive the first- and second-order reflection signals from the wall, floor, ceiling, table or other indoor objects when a person or an object blocks the LOS communication link. Literature [21] proposed an analysis method for the DC gain of the first-order and second-order wall reflections, considering all possible reflection possibilities along the propagation path.

The blue dotted line in Fig. 1(a) is the LOS communication boundary line considering the shadowing effect of the person. In the area above the boundary line, LOS communication can be realized. However, in this work, we assume that the receiver is located below the boundary line, and the light can reach the receiver mainly after the first-order reflection. In the communication scenario in Fig. 1(a), the main propagation paths from the LED to the receiver include the reflections from four walls, ground and other indoor objects such as table. The optical power received by the receiver can be expressed as:

$$P_{r-nlos} \approx H_1(0)P_t. \tag{2}$$

In this case, we only consider the VLC up to the first-order reflection.

Furthermore, we consider a smart device such as a sweeping robot under the table shown in Fig. 1(b). In this scenario, in most cases the light can reach the receiver at most after two reflections when the LOS link is interrupted. For the propagation from the first-order reflection, light travels from the LED to one of the four walls or ground, and after the reflection it reaches the receiver. For the propagation from the second-order reflection, the light propagation between different surfaces exists. The different combinations of these propagation paths between different surfaces can lead to four light propagation types as shown in Fig. 1(b). As shown in Fig. 1(b), the light travels from the LED to the walls and floor, and then is reflected from the walls and table before reaching the

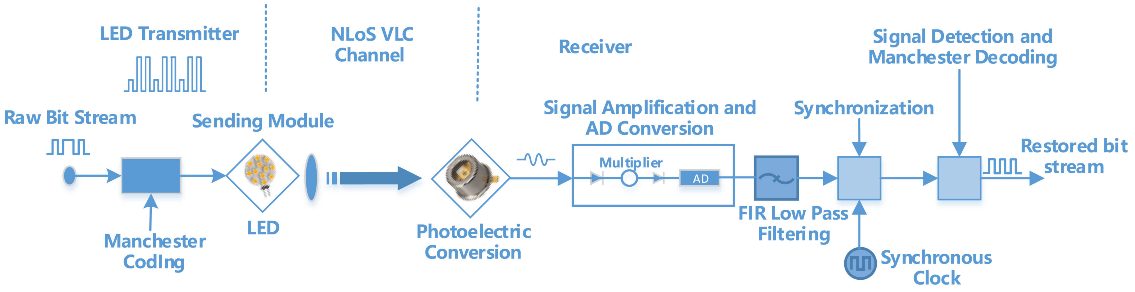

Fig. 2. The communication system diagram of NLOS VLC.

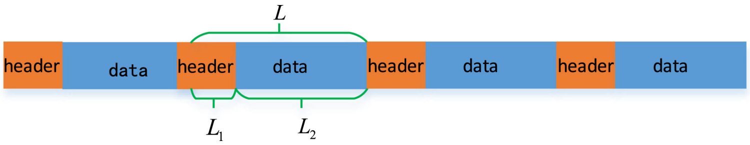

Fig. 3. The data stream with periodical synchronization code.

receiver. If the APD-based receiver points upward to the table or to the wall, and the half power angle of the LED is small, the signals from the first-order reflection is negligible and that from the second-order reflections dominates. The optical power at the receiver can be expressed as:

$$P_{r-nlos} \approx H_2(0)P_t. \tag{3}$$

In this case, we only consider the VLC up to the second-order reflection.

3. Signal Processing

The block diagram of an NLOS reflection-based visible light communication system is shown in Fig. 2. The system consists of the transmission part, the NLOS channel, and the receiving part. At the transmitter, Manchester coding is adopted to modulate the optical signal intensity. The light wave carrying the transmitted data reaches the receiver through the NLOS reflection link. At the receiver, the APD converts the detected optical signal to electrical signal, after which the binary bits are recovered through analog-to-digital conversion, finite impulse response (FIR) low-pass filtering, synchronization, detection and Manchester decoding. Note that the Manchester code is adopted to suppress the low-frequency components of the transmitter-side electrical signal, and thus alleviates the impairments of the transmitter-side bias-tee.

After the ADC, the receiver side first performs Chebyshev low-pass filter, to remove the high-frequency noise. The filtering output is processed for synchronization and symbol detection.

3.1 Sliding Based Synchronization

We consider periodically inserting the synchronization pilots modulated by On-Off Keying (OOK), as shown in Fig. 3. The receiver performs a sliding-window correlation on the received signal to find the correlation peaks, i.e., find the “start” positions of a frame.

Literature [22] proposed that in case of low signal-to-noise ratio (SNR), a large number of synchronization identifiers need to be periodically inserted in order to achieve the required synchronization accuracy. Increasing the length of the identification code can improve the synchronization performance of the receiver, but results in lower bandwidth utilization. Aligned with the weak signal nature of the NLOS reflection channel, in this work we improve synchronization performance by increasing the sampling rate.

Assume that $s = \{s[k]\}_{k=1}^{K}$ and $s_{sync} = \left\{s_{sy}[k]\right\}_{k=1}^{L_1}$ represent the transmitted symbols of and the inserted synchronization symbols, respectively, $r = \{r[k]\}_{k=1}^{NK}$ and $r_{sy} = \left\{r_{sync}[k]\right\}_{k=1}^{NL_1}$ represent the received samples of a frame and the inserted synchronization symbols at N times sample rate, respectively. The sliding correlation value is expressed as:

$$R[i] = \frac{\sum_{j=1}^{NL_1} r_{sy}[j] r[i+j]}{\left(\sum_{j=1}^{NL_1} (r_{sy}[j])^2\right)^{\frac{1}{2}} \left(\sum_{j=1}^{NL_1} (r[i+j])^2\right)^{\frac{1}{2}}}, \quad 1 \le i \le N(K - L_1). \tag{4}$$

3.2 Gaussian Approximation-Based Detection With Manchester Coding

We introduce conventional detection for Manchester coded signal with N times oversampling, which is used as the performance comparison benchmark. For channel estimation, let x_j denote the *j-th* pilot symbol, Y_j denote the mean sample of the *j-th* synchronization symbol. Let $\mathcal{X}_0 \triangleq \{j, x_j = 0\}$ and $\mathcal{X}_1 \triangleq \{j, x_j = 1\}$ represent the set of positions of symbol 0 and symbol 1 in the synchronization pilots, respectively. Then, assume Y_j obeys the following Gaussian distribution, which is given by Eq. (5). The mean and variance estimates, denoted as $\hat{\mu}_0$, $\hat{\mu}_1$, $\hat{\sigma}_0^2$, $\hat{\sigma}_1^2$ for symbols zero and one, respectively, are given by Eq. (6).

$$\begin{aligned} &Y_j \sim N(\hat{\mu}_0, \hat{\sigma}_0^2), x_j = 0; \\ &Y_j \sim N(\hat{\mu}_1, \hat{\sigma}_1^2), x_j = 1. \end{aligned} \tag{5}$$

$$\begin{aligned} \hat{\mu}_0 &= \frac{\sum_{j \in \mathcal{X}_0} Y_j}{|\mathcal{X}_0|}; \quad \hat{\sigma}_0^2 = \frac{\sum_{j \in \mathcal{X}_0} (Y_j - \hat{\mu}_0)^2}{|\mathcal{X}_0|}; \\ \hat{\mu}_1 &= \frac{\sum_{j \in \mathcal{X}_1} Y_j}{|\mathcal{X}_1|}; \quad \hat{\sigma}_1^2 = \frac{\sum_{j \in \mathcal{X}_1} (Y_j - \hat{\mu}_1)^2}{|\mathcal{X}_1|}. \end{aligned} \tag{6}$$

Then, for symbols 0 and 1, each mean sample r_k obeys the conditional distribution shown by Eq. (7). For Manchester coding, the Gaussian approximation-based detection is given by Eq. (8). The *m-th* original symbol is detected as one if and only if the corresponding Logarithm Likelihood Ratio (LLR) is larger than or equal to zero.

$$p(r_k|0) = \frac{1}{\sqrt{2\pi\hat{\sigma}_0^2}} e^{-\frac{(r_k - \hat{\mu}_0)^2}{2\hat{\sigma}_0^2}}, \quad p(r_k|1) = \frac{1}{\sqrt{2\pi\hat{\sigma}_1^2}} e^{-\frac{(r_k - \hat{\mu}_1)^2}{2\hat{\sigma}_1^2}}. \tag{7}$$

$$\begin{aligned} LLR(m) &= \ln \frac{p(r_{2m}|1) p(r_{2m-1}|0)}{p(r_{2m}|0) p(r_{2m-1}|1)} \\ &= \frac{(r_{2m} - \hat{\mu}_0)^2 - (r_{2m-1} - \hat{\mu}_0)^2}{2\hat{\sigma}_0^2} + \frac{(r_{2m-1} - \hat{\mu}_1)^2 - (r_{2m} - \hat{\mu}_1)^2}{2\hat{\sigma}_1^2}. \end{aligned} \tag{8}$$

3.3 Support Vector Machine-Based (SVM) Detection

For practical visible light communication systems, the received waveform is seriously distorted by imperfect transceivers. Such nonlinear distortion impedes accurate modeling based on statistical signal framework. Thus, we resort to learning-based approach. In this work, we adopt support vector machine-based detection for the NLOS optical signals.

We conduct experiments to demonstrate the sample features of pulses "0" and "1". The APD receiver is placed below the table pointing to the wall, and the DC voltage of bias-tee is set to 36.5 V and the AC voltage is set to 900 mV. The LED is put on the ceiling (245 cm above the ground).

The red dots in Figs. 4(a)(b)(c) and Figs. 4(d)(e)(f) show the ten samples corresponding to pulse "0" and pulse "1", respectively. Note that there are three types of symbol "0" for Manchester coding, the first "0" in two consecutive "00", the second "0" in two consecutive "00", and the "0" in "101".

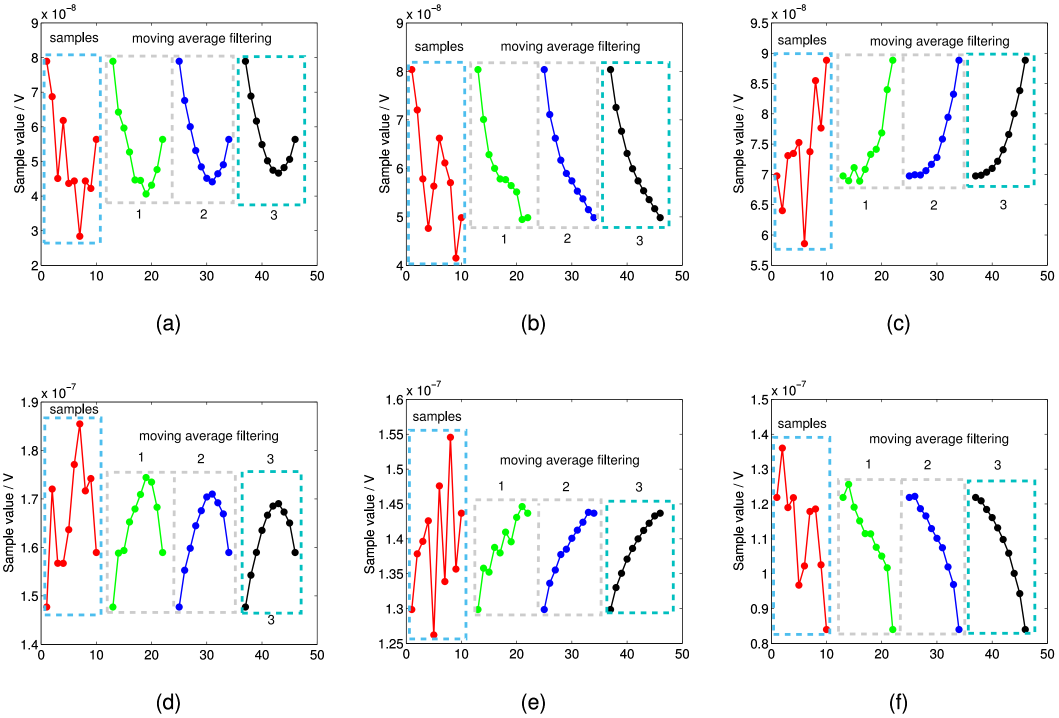

(a) (b) (c)

(d) (e) (f)

Fig. 4. Signal features extraction and recovery.

The green, blue and black dots are the samples after one-time, two-time and three-time moving average filtering, respectively. It can be seen from Fig. 4 that moving average filtering can recover the features of the received signals. In Fig. 4(a), the black dots first move down and then move up, whose second derivation is below zero and then above zero. In Fig. 4(b), the black dots keep moving down, whose second derivation is below zero. In Fig. 4(c), the black dots move up, whose second derivation is greater than zero. In Fig. 4(d), the black dots first move up and then move down, whose second derivation is below zero and then above zero. In Fig. 4(e), the black dots move up, whose second derivation is below zero. In Fig. 4(f), the black dots move down, whose second derivation is greater than zero. Therefore, we can also utilize the first derivative and second derivative of the sample values, as well as the mean sample and mean sample LLR, to detect zero pulse and one pulse.

We propose a detection method based on SVM shown in Fig. 5. Firstly, we let $\hat{X}_i = \{\hat{x}_i^k\}_{k=1}^N$, $i = 1, 2, 3, ..., K$ denote the set of samples of the received signal corresponding to the $i-$th pulse after FIR filtering. Then, the moving average filtering can be calculated as:

$$x_i^k = \begin{cases} \hat{x}_i^k, k = 1 \text{ or } N; \\ (\hat{x}_i^{k-1} + \hat{x}_i^k + \hat{x}_i^{k+1})/3, k = 2 \text{ or } k = N - 1\,; \\ (\hat{x}_i^{k-2} + \hat{x}_i^{k-1} + \hat{x}_i^k + \hat{x}_i^{k+1} + \hat{x}_i^{k+2})/5, \text{ otherwise.} \end{cases} \tag{9}$$

Let v_i denote the feature vector of the samples of the *i-th* pulse, given by Eq. (10), where parameters μ_i, LLR_i, $d_{1,i}^{(1)}$, $d_{2,i}^{(1)}$, $d_{3,i}^{(1)}$, $d_{4,i}^{(1)}$, $d_{1,i}^{(2)}$ and $d_{2,i}^{(2)}$ are stacked into the following feature,

$$v_i = \left[\mu_i, LLR_i, d_{1,i}^{(1)}, d_{2,i}^{(1)}, d_{3,i}^{(1)}, d_{4,i}^{(1)}, d_{1,i}^{(2)}, d_{2,i}^{(2)}\right]. \tag{10}$$

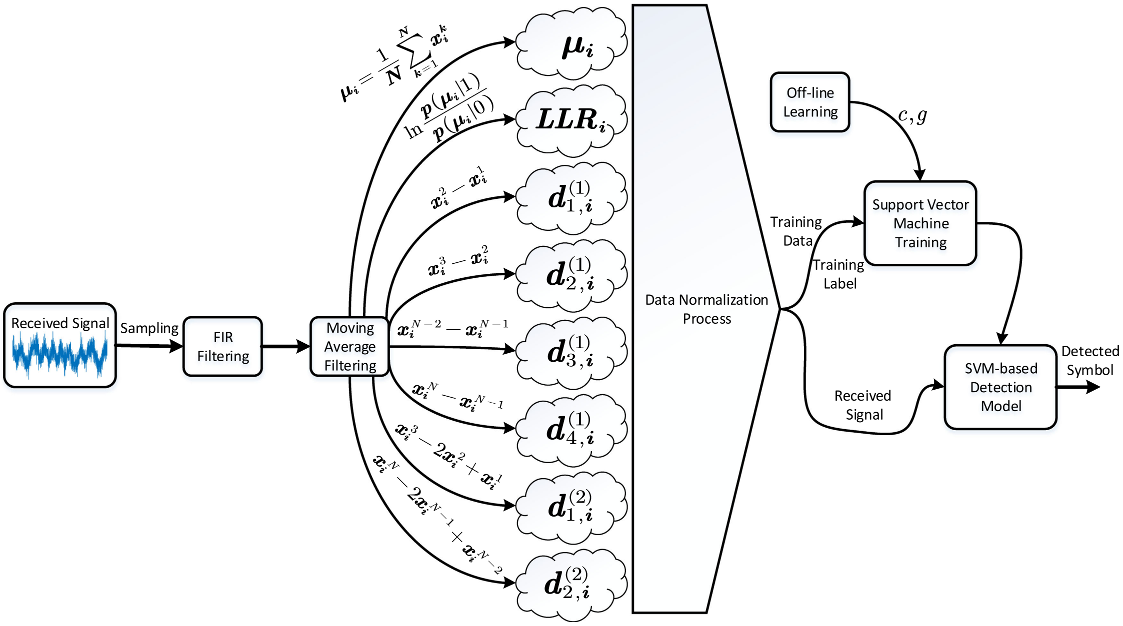

Fig. 5. Support Vector Machine-based (SVM) Detection Diagram.

$$
\begin{aligned}
&\mu_i = \frac{1}{N}\sum_{k=1}^{N} x_i^k, && LLR_i = \ln\frac{p(\mu_i|1)}{p(\mu_i|0)},\\
&d_{1,i}^{(1)} = x_i^2 - x_i^1, && d_{2,i}^{(1)} = x_i^3 - x_i^2,\\
&d_{3,i}^{(1)} = x_i^{N-1} - x_i^{N-2}, && d_{4,i}^{(1)} = x_i^N - x_i^{N-1},\\
&d_{1,i}^{(2)} = x_i^3 - 2x_i^2 + x_i^1, && d_{2,i}^{(2)} = x_i^N - 2x_i^{N-1} + x_i^{N-2}.
\end{aligned}
\tag{11}
$$

SVM is designed to find function $y_i^{'} = f(v_i)$ that approximates pulse detection. The error between the predicted value $y_i^{'}$ and the true value y_i is minimized by SVM algorithm. Radial Basis Kernel Function (RBF) is adopted for its outstanding performance in vast majority of occasions, given by

$$\Phi(v_i) = e^{-g\cdot|v_i-\lambda|^2}, \tag{12}$$

where g is the kernel parameter of the Gaussian function; λ is the center of the RBF kernel function; v_i is the feature vector of the samples of known pulses, which is serve as the training data in the SVM detection, while the corresponding transmitted pulse "0" and pulse "1" are inputted as the training label.

The objective function and constraints of the SVM optimization are given by:

$$
\begin{aligned}
&\min_{w} \frac{1}{2}\|w\|^2 + C\sum_{i=1}^{n}\xi_i\\
&\text{s.t.}\quad y_i\left(w^T\Phi(v_i) + b\right) \geqslant 1 - \xi_i\,,\ \ i = 1, 2, \ldots, K\,.
\end{aligned}
\tag{13}
$$

In the SVM optimization problem, y_i is the training label; v_i is the feature vector which has been normalized; $\Phi(v_i)$ is a kernel function of the feature vector; w is the weighting vector; ξ_i is the relaxation factor; C is the penalty factor; b means a constant term. In the SVM model training process, optimization of parameters C and g can further improve the performance, which can be learned off-line. Parameter C is a trade-off of the appropriate relaxation of the margin size and tolerance of classification errors. It weighs the empirical risk and structural risk, where larger C

leads to smaller empirical risk, larger structural risk, and easier over-fitting; while smaller C leads to lower complexity, and easier under-fitting. There also exists a trade-off on the kernel function hyper-parameter g. It is related to the granularity of the data sample, where smaller g leads to more complex curve selected in the low-dimensional space, finer classification, and easier over-fitting. Larger g leads to thicker classification, which may result in the inability to distinguish data, which is prone to under-fitting. We perform grid search to optimize parameters C and g. The finite set of parameters are given by

$$\begin{aligned}
&C \in \left\{2^{-a_1}, 2^{-a_1+b_1}, 2^{-a_1+2b_1}, \ldots, 2^{-a_1+(n-1)b_1}, 2^{a_1}\right\},\\
&g \in \left\{2^{-a_2}, 2^{-a_2+b_2}, 2^{-a_2+2b_2}, \ldots, 2^{-a_2+(n-1)b_2}, 2^{a_2}\right\},\\
&a_1 = \frac{nb_1}{2}, \ a_2 = \frac{nb_2}{2},
\end{aligned} \tag{14}$$

where a_1 and a_2 are the thresholds of the parameters and b_1 and b_2 denote the span values of the grid.

4. Experimental Results on the NLOS Reflection VLC

4.1 Experimental System Realization

At the transmitter side, a Rigol DG5252 arbitrary waveform generator (AWG) is used to generate random data and drive the commercial Philips LED using OOK modulation, where the power is supplied by a bias-tee. Note that one frame has a length of 4096 and its pilot's length is 511. At the receiver side, the optical signal is detected using Hamamatsu C12702 series APD with DC and low-pass filtering. The OPHIR Photonics Nova II P/N 7Z01550 optical power meter is employed to measure the received optical power and calculate the power on the detector surface based on the ratio of the detector area over power meter area. The APD output signal is captured and saved using an Agilent MSOX6004A oscilloscope for further offline processing in the computer. The experimental system is shown in Fig. 6(a). The OOK signal is amplified by a MINI-CIRCUITS ZHL-6A-S+ power amplifier and input to a MINI-CIRCUITS ZFBT-4R2GW+ bias-tee. We set the DC voltage of bias-tee to 37.5 V and AC voltage to 900 mV. Finally, the output signal of the bias-tee is used to drive the LED to transmit optical signals. The bias-tee pass band is 0.1–4200 MHz, and can offer power up to 30 dBm.

First, we adopt OOK modulation in our experiments. In order to test the output signal after photoelectric conversion, we use an APD pointing to the LED and set the communication distance to 2 m. The received signals with symbol rate 2 Mbps and 4 Mbps after photoelectric conversion are shown in Fig. 7(a) and Fig. 7(c), respectively, which are seriously distorted due to the low frequency cutoff of the bias-tee. To solve this issue, we encode the OOK signal using Manchester coding, i.e., symbol zero is encoded into “1 0” pulses, and symbol one is encoded into “0 1” pulses. The received signals with pulse width 0.25 μs and 0.125 μs after photoelectric conversion are shown in Fig. 7(b) and Fig. 7(d), respectively, which are significantly less distorted than that without Manchester coding. Note that the labeled bit streams in Fig. 7 are not coded by Manchester coding, corresponding to the waveform in the region. Note that although there exists multi-path from reflections from walls and floors, the time dispersion in the room is within 20 ns, which is small compared with the symbol duration. Thus, the inter-symbol interference is not considered in this work.

4.2 Signal Analysis

We conduct experiments to demonstrate the characteristic of the received signal after FIR low-pass filtering. Note that the OOK signal is encoded by Manchester coding. Fig. 8(a) shows the eye diagram for the first-order reflection signal at bit rate 8 Mbps. The APD receiver is placed on the table pointing to the wall in the position $(x, y) = (-1, 0.8)(m)$, and the DC voltage of bias-tee is set

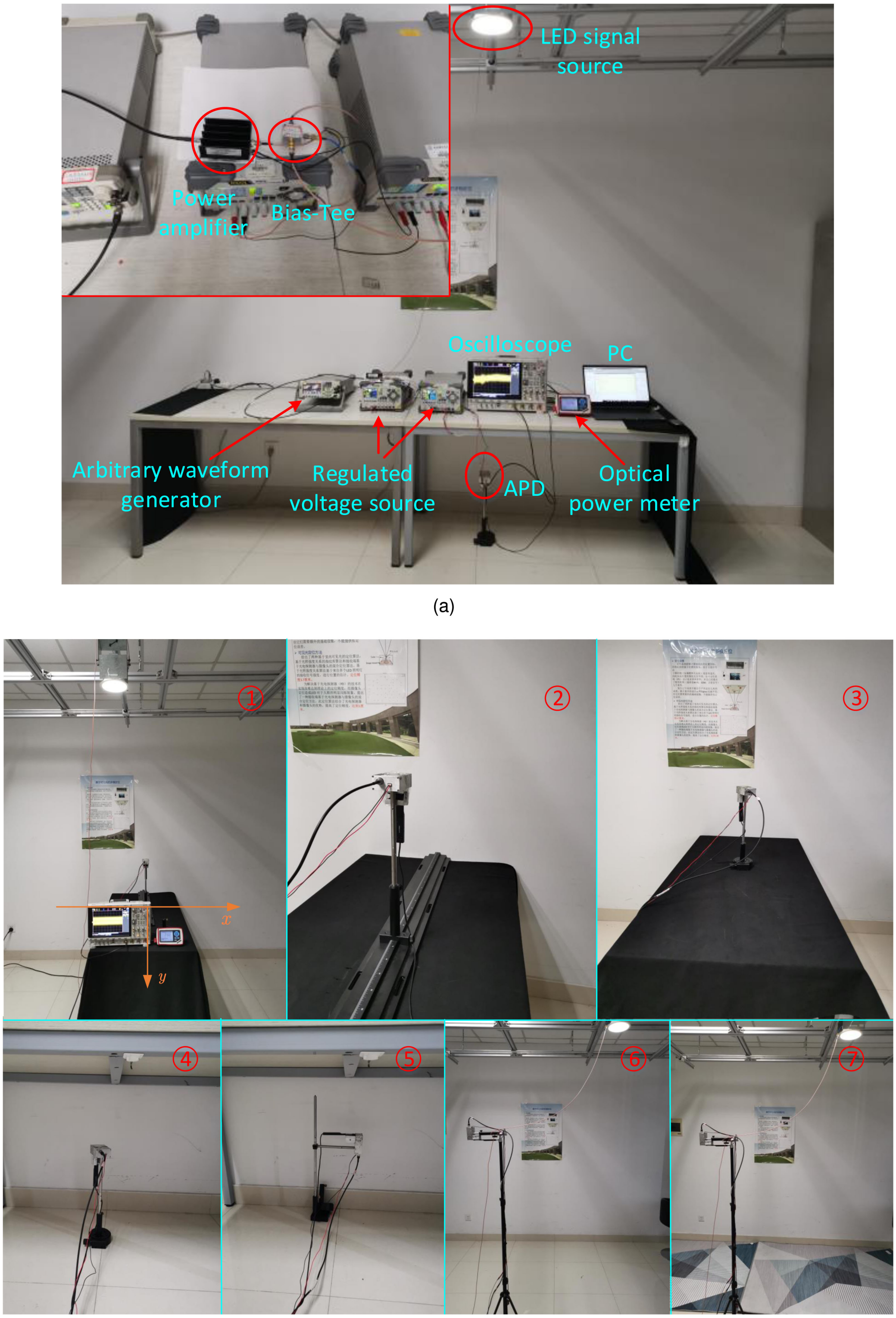

(a)

(b)

Fig. 6. The experimental system and environment. (a) The experimental system. (b) The experimental system environments.

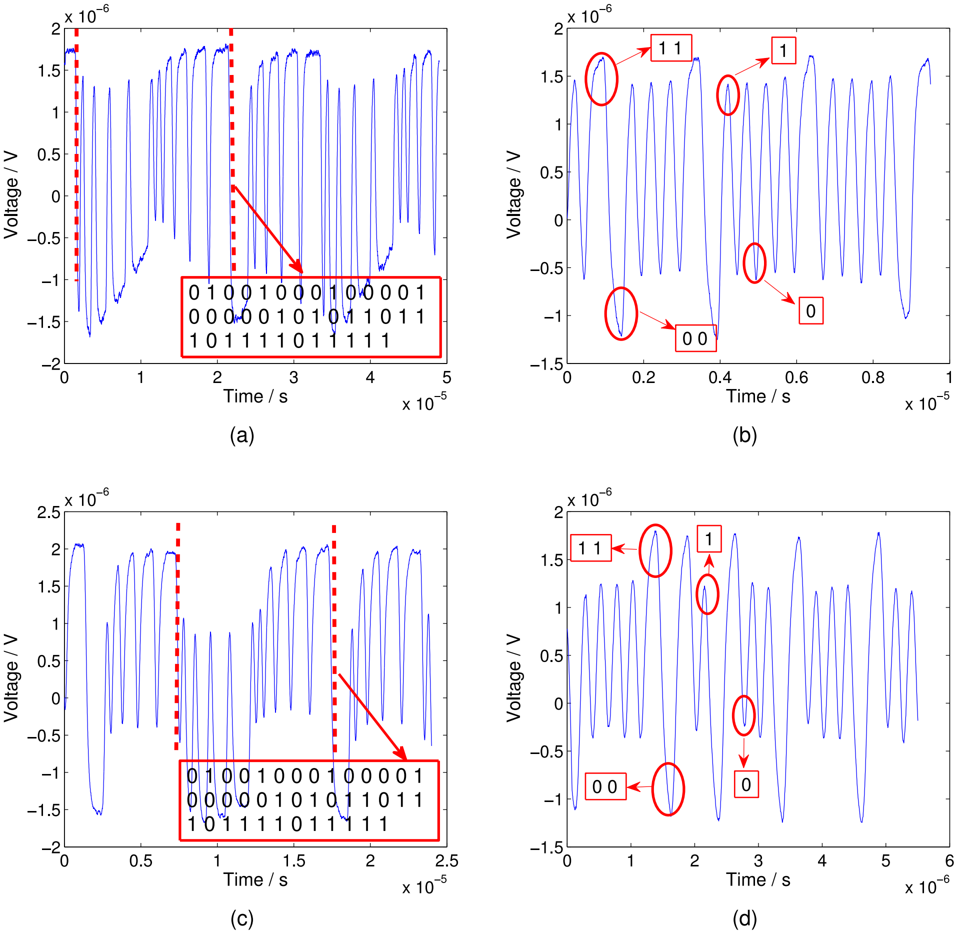

(a)

(b)

(c)

(d)

Fig. 7. The received signals after photoelectric conversion. (a) The received signal with symbol rate 2 Mbps after photoelectric conversion without Manchester coding. (b) The received signal with pulse width 0.25 μs after photoelectric conversion with Manchester coding. (c) The received signal with symbol rate 4 Mbps after photoelectric conversion without Manchester coding. (d) The received signal with pulse width 0.125 μs after photoelectric conversion with Manchester coding.

to 37.5 V and the AC voltage is set to 900 mV. Fig. 8(b) shows the eye diagram for the second-order reflection signal at bit rate 4 Mbps, where the APD receiver is placed below the table pointing to the wall in the position $(x, y) = (-1, 0.3)(m)$. We can see that the eye diagrams are vague due to strong signal attenuation and ambient noise, where the learning-based signal detection may outperform the simple sampling-and-average detection. Moreover, the eye diagram in Fig. 8(b) is clearer than that in Fig. 8(a) due to lower bit rate 4 Mbps.

4.3 Grid Search

The discussion in Section 3.3 implies that the estimation performance is determined by parameters C and g, which represent penalty coefficient and kernel function parameter in the SVM, respectively. We investigate the performance with respect to parameters C and g. The training data is the output signal samples after FIR filtering and moving average filtering with the APD receiver at different locations in the room, while the training label is the corresponding pulse “0” or pulse “1”. We divide the samples into five parts, and conduct five times of training and verification processes. Each time four parts are used for training and one part is used for testing. The average prediction accuracy

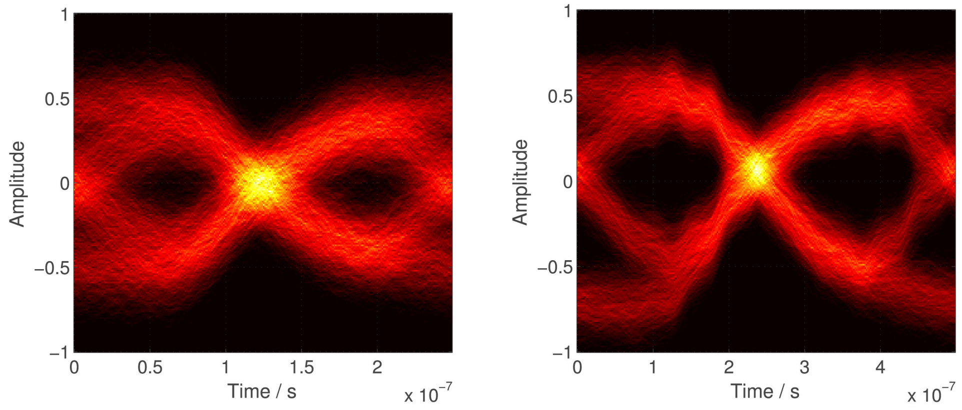

(a)

(b)

Fig. 8. The eye diagrams of the received signal after FIR low-pass filtering. (a) The eye diagram of the received first-order reflection signal after FIR low-pass filtering. (b) The eye diagram of the received second-order reflection signal after FIR low-pass filtering.

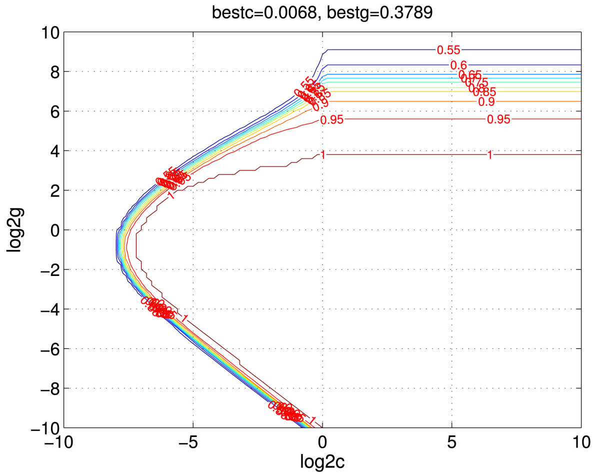

Fig. 9. Grid search for optimal *C* and *g*.

is adopted as the metric. The prediction accuracy of the SVM detection model is calculated and displayed in Fig. 9. It is seen that the optimal *C* and *g* are 0.0068 and 0.3789, respectively.

4.4 Experimental Results on the First-Order Reflection for the Receiver on the Table and Towards the Wall

We compare the performance of the proposed SVM detection method with that of the conventional Gaussian approximation-based detection method for the indoor VLC after the first-order reflection at bit rate 8 Mbps. We conducted the experiments shown in the subplots marked as 1 and 2 in Fig. 6(b), where the receiver is on the table and points to the wall, and mainly receives the first-order reflection signals from the wall and floor. In order to guarantee negligible received signals from the table reflection, we placed one black cloth on the table. Assume the direction of LED pointing to the wall is *y*-axis and the perpendicular direction is the *x*-axis, the same directions as those the subplot marked as 1 in Fig. 6(b).

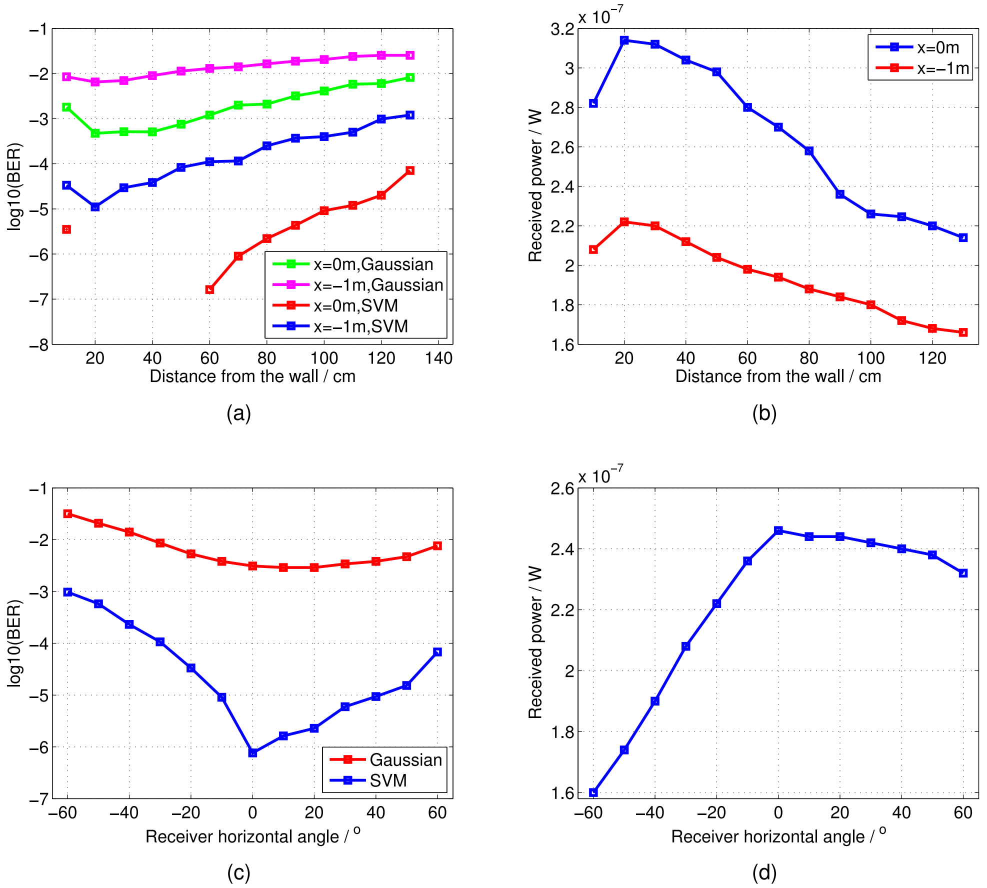

Fig. 10. The detection error rates and received power on the first-order reflection for the receiver on the table and towards the wall. (a) The detection error rates at different locations on the table (zero BER for $x = 0$ m and distance between 10 cm and 60 cm). (b) The received optical power at different receiver locations on the table. (c) The detection error rates for different receiver horizontal angles on the table. (d) The received optical power for different receiver horizontal angles on the table.

The LED and APD receiver are on the ceiling (245 cm above the ground) and on the table (110 cm above the ground), respectively. The received optical power at different locations shown in Fig. 10(b) and the corresponding detection error rates are shown in Fig. 10(a). The curves labeled by "$x = 0$ m" and "$x = -1$ m" represent the receiver x-axis coordinates are 0 m and −1 m, respectively, where the LED projection on the floor is at x coordinate zero. The curves labeled by "Gaussian" and "SVM" represent the Gaussian approximation-based detection and SVM detection, respectively. It can be seen from Fig. 10(a) that the BERs of both Gaussian approximation-based detection and SVM detection first decrease and then increase as the distance between the receiver and the wall increases. The reason is that the received power first increases and then decreases. Moreover, the BERs of the SVM detection are lower by at least one order of magnitude than that of the Gaussian approximation-based detection and reach 10^{-3}.

Fig. 10(c) shows the BERs for different horizontal angles of receiver direction given fixed receiver position $(x, y) = (0, 0.6)(m)$ on the table. The experiment setup is shown in the subplot marked as 3 in Fig. 6(b). We can see that the BERs first decrease and then increase as the receiver horizontal angle increases, where the corresponding received power is shown in Fig. 10(d). We can see that the BERs of the SVM detection are lower by at least one order of magnitude than that of the Gaussian approximation-based detection and reach 10^{-3}. Moreover, the asymmetric performance of positive and negative angles in Figs. 10(c)(d) can be justified by an iron cabinet on the right

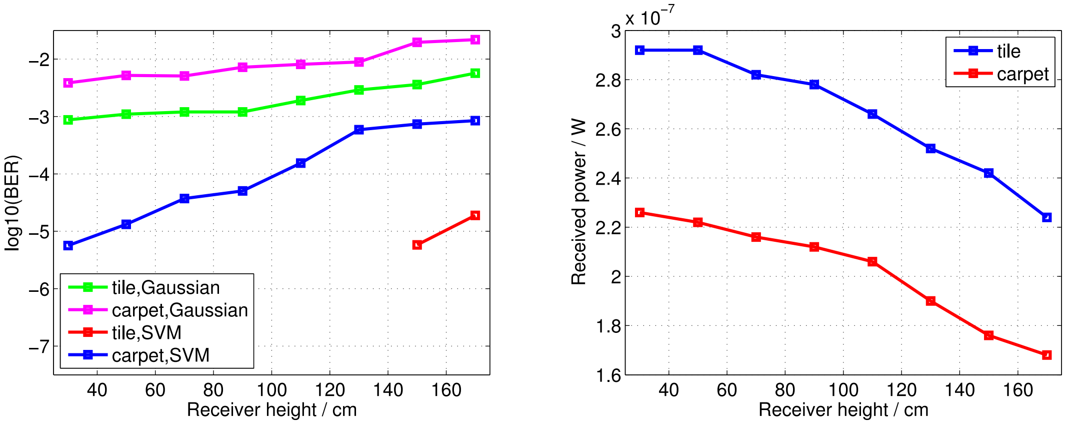

(a) (b)

Fig. 11. The detection error rates and received power on the first-order reflection for the receiver towards the tiles and carpet. (a) The detection error rates with different receiver heights (zero BER for tile with height below 150 cm). (b) The received power with different receiver heights.

side of the room, which can reflect the light to the receiver and leads to asymmetric distribution of ambient light in positive and negative angles.

4.5 Experimental Results on the First-Order Reflection for the Receiver Towards the Tile and Carpet

We further study the performance of the proposed SVM detection for indoor VLC after the first-order reflection with bit rate 8 Mbps. We conducted experiment shown in the subplots marked as 6 and 7 in Fig. 6(b), where the receiver points to the ground and mainly receives the first-order reflection signals from the tiles and carpet, respectively. Note that the receiver and LED are on the same horizontal line and the distance between them is 1 m.

The received optical power at different locations is shown in Fig. 11(b) and the corresponding detection error rates with different receiver heights are shown in Fig. 11(a). The curves labeled by “Gaussian” and “SVM” represent the Gaussian approximation-based detection and SVM detection, respectively. The curves marked by “tile” and “carpet” represent the ground reflection by tile and carpet, respectively. It can be seen from Fig. 11(a) that the BERs of both Gaussian approximation-based detection and SVM detection increase with the receiver height due to the decreased the received power. Moreover, the BERs of the SVM detection are lower by at least one order of magnitude than that of the Gaussian approximation-based detection and reach 10^{-3}.

4.6 Experimental Results on the Second-Order Reflection for the Receiver Under the Table and Towards the Table

We study the performance of the proposed SVM detection method and compare it with conventional Gaussian approximation-based detection method for the indoor VLC after the second-order reflection with bit rate 4 Mbps. The experiment is shown in the subplot marked as 5 in Fig. 6(b), where the receiver with position $(x, y) = (0, 0.1)(m)$ under the table points to the table, and the LED projection center on the floor is at x coordinate 0 m. In order to guarantee no LOS link, we placed the receiver on the shaded area under the table. Thus the receiver receives the second-order reflection signals primarily from the wall and the table.

Fig. 12(a) shows the corresponding detection error rates for different receiver heights. The corresponding optical power is shown in Fig. 12(b). The curves marked by “x = 0 m” and “x = −1 m” represent that the x coordinates of the receiver are 0 m and −1 m, respectively. The curves

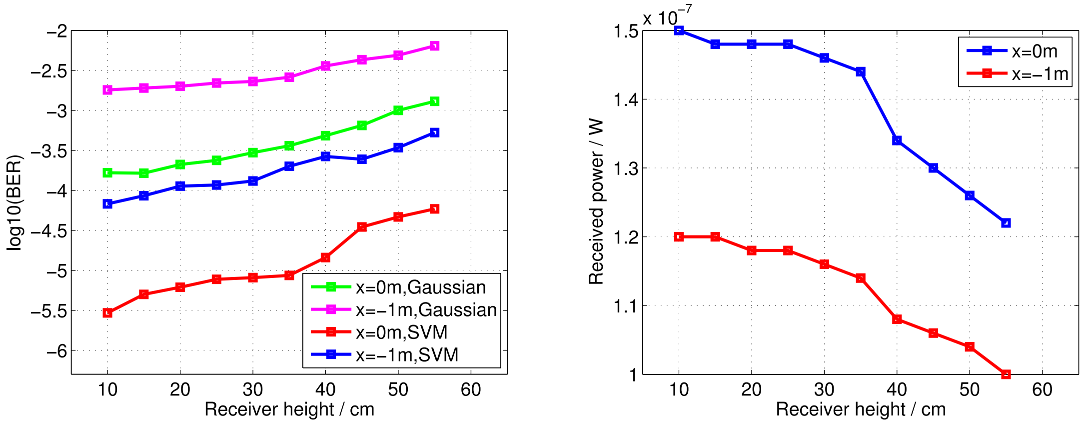

(a) (b)

Fig. 12. The detection error rates and received power for the receiver under the table and towards up to the table. (a) The detection error rates with different receiver heights under the table. (b) The received power with different receiver height under the table.

labeled by “Gaussian” and “SVM” represent the Gaussian approximation-based detection and SVM detection, respectively. It can be seen from Fig. 12(a) that the BERs increase with the height of the receiver as the received power decreases. Moreover, the BERs of the SVM detection are lower by at least two orders of magnitude than that of the Gaussian approximation-based detection and below 10^{-3}.

4.7 Experimental Results on the Second-Order Reflection for the Receiver Under the Table and Towards the Wall

We further investigate the performance of the SVM detection method for the second-order reflection indoor VLC with bit rate 4 Mbps. In the communication scenario shown in Fig. 6(a), we put the LED on the ceiling (245 cm above the ground) and the APD receiver under the table. The receiver points towards the wall inside at the height 35 cm. In order to ensure that the main received signals are from the second-order reflection from the wall and table, we placed two black cloths at the edge of the table.

The detection error rates at different locations are shown in Fig. 13(a), and the corresponding received optical power is shown in Fig. 13(b). The curves marked by “x $= 0$ m” and “x $= -1$ cm” represent that the x coordinates of the receiver are 0 m and -1 m, respectively. The curves labeled by “Gaussian” and “SVM” represent the Gaussian approximation-based detection and SVM detection, respectively. It can be seen that the BERs of both Gaussian approximation-based detection and SVM detection first increase and then decrease with the increase of the distance between the receiver and the wall. The reason is that the received power first decreases and then increases. We can also see from Fig. 13(a) that the BERs of the SVM detection are lower by at least two to orders of magnitude than that of the Gaussian approximation-based detection, and below 10^{-4}.

Fig. 13(c) shows the BERs for different horizontal angles of receiver direction given fixed receiver position $(x, y) = (0, 0.35)(m)$ under the table. The experiment setup is shown in the subplot marked as 4 in Fig. 6(b). We can see that the BERs first decrease and then increase as the receiver horizontal angle increases, where the corresponding received power is shown in Fig. 13(d). It can be seen that the BERs of the SVM detection are lower by one to two orders of magnitude than that of the Gaussian approximation-based detection and below 10^{-3}. Moreover, the transmission performance of positive and negative angles is asymmetric in Fig. 13(c)(d). This can be justified by

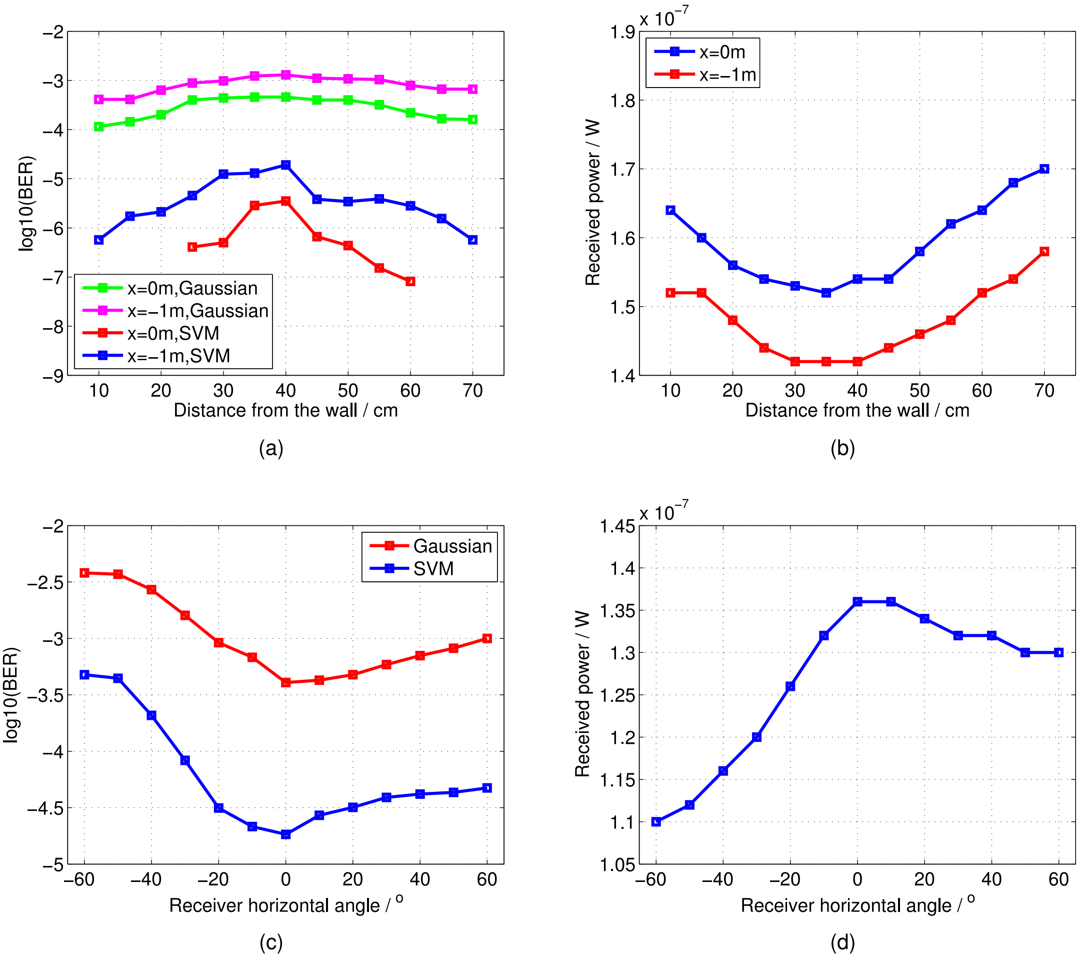

Fig. 13. The detection error rates and received power on the second-order reflection for the receiver under the table and towards the wall. (a) The detection error rates at different locations under the table. (b) The received optical power at different receiver locations under the table. (c) The detection error rates for different receiver horizontal angles under the table. (d) The received optical power for different receiver horizontal angles under the table.

the fact that other objects in the room are placed asymmetrically and lead to asymmetric distribution of ambient light in positive and negative angles in Fig. 13(c)(d).

4.8 Experimental Results on the Second-Order Reflection for the Receiver Under the Table and Towards the Wall at Different Transmission Rates

We place the receiver at position $(x, y) = (0, 0.35)(m)$ under the table to study the performance of the SVM detection in the second-order reflection communication for the receiver under the table and towards the wall at different transmission rates. Fig. 14 shows the BERs of the SVM detection and Gaussian approximation-based detection at bit rates from 0.4 Mbps to 5 Mbps. The curves marked by "5 times" and "10 times" represent the sample rates of 5 times and 10 times oversampling, respectively. The curves labeled by "Gaussian" and "SVM" represent the Gaussian approximation-based detection and SVM detection, respectively. It can be seen that the BERs of both Gaussian approximation-based detection and SVM detection first decrease and then increase with the increase of the transmission rate due to low-frequency cutoff of the transmitter-side bias-tee. We can also see that the SVM detection with 10 times oversampling shows lower BER than the

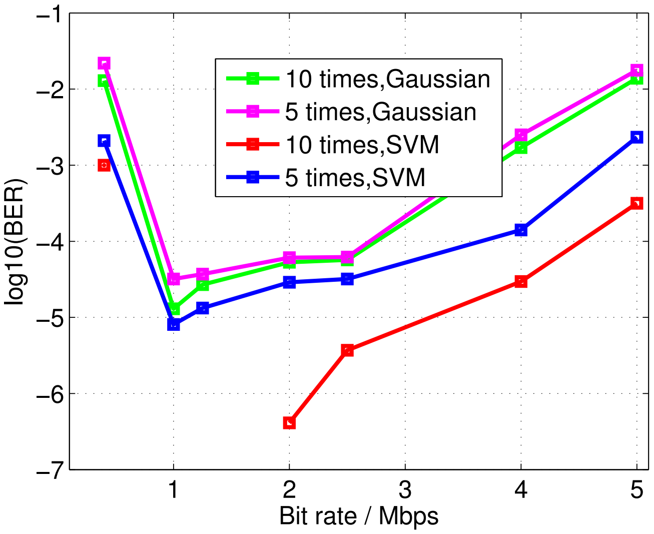

Fig. 14. The detection error rates for the receiver under the table and towards the wall at different bit rates.

Gaussian approximation-based detection. Moreover, Fig. 14 shows that high-sampling can improve the performance of the SVM detection more significantly.

5. Conclusions

We have considered the NLOS visible light communication from the wall and floor reflection, and proposed an SVM detection method and compared it with the conventional Gaussian approximation-based detection method. Experimental results show that proposed detection has significant performance improvement. We have conducted experiments to compare the performance of the SVM detection and Gaussian approximation-based detection, and demonstrated the feasibility of indoor NLOS VLC from the wall, floor and table reflections up to the second order. It is demonstrated from experimental results that the indoor NLOS VLC can maintain a reliable link for bit rate up to 8 Mbps with Manchester coding. Under the first-order reflection, the BERs of the SVM detection for the receiver on the table and towards the wall at bit rate 8 Mbps can be reduced at least one order of magnitude compared with the Gaussian approximation-based detection, and can reach 10^{-3}. The BERs of the SVM detection for the receiver towards the ground at bit rate 8 Mbps can also be reduced at least one order of magnitude compared with the Gaussian approximation-based detection, and can reach 10^{-3}. Under the second-order reflection, the BERs of the SVM detection for the receiver under the table and towards the wall at bit rate 4 Mbps can be reduced at least two orders of magnitude compared with the Gaussian approximation-based detection, and can reach 10^{-4}. The BERs of the SVM detection for the receiver under the table and towards the table at bit rate 4 Mbps can also be reduced at least two orders of magnitude compared with the Gaussian approximation-based detection, and can below 10^{-3}.

References

[1] Y. Wang, N. Chi, Y. Wang, L. Tao, and J. Shi, “Network architecture of a high-speed visible light communication local area network,” *IEEE Photon. Technol. Lett.*, vol. 27, no. 2, pp. 197–200, Jan. 2015.

[2] N. Chi, Y. Zhou, S. Liang, F. Wang, J. Li, and Y. Wang, “Enabling technologies for high-speed visible light communication employing CAP modulation,” *IEEE J. Lightw. Technol.*, vol. 36, no. 2, pp. 510–518, Jan. 2018.

[3] N. Chi, H. Haas, M. Kavehrad, and T. D. C. Little, and X. Huang, “Visible light communications: demand factors, benefits and opportunities,” *IEEE Wireless Commun.*, vol. 22, no. 2, pp. 5–7, Apr. 2015.

[4] H. Qian, S. Cai, S. Yao, T. Zhou, Y. Yang, and X. Wang, “On the benefit of DMT modulation in nonlinear VLC systems,” *Opt. Exp.*, vol. 23, no. 3, pp. 2618–2632, 2015.

[5] M. Biag, T. Borogovac, and T. D. C. Little, “Adaptive receiver for indoor visible light communications,” *IEEE J. Lightw. Technol.*, vol. 31, no. 23, pp. 3676–3686, Dec, 2013.

[6] S. Dimitrov, S. Sinanovic, and H. Haas, “Signal shaping and modulation for optical wireless communication,” *IEEE J. Lightw. Technol.*, vol. 30, no. 9, pp. 1319–1328, May 2012.

[7] D. Tsonev, S. Videv, and H. Haas, “Towards a 100 Gb/s visible light wireless access network,” *Opt. Exp.*, vol. 23, no. 2, pp. 1627–1637, 2015.

[8] A. A. Alatawi *et al.*, “High-power blue superluminescent diode for high CRI lighting and high-speed visible light communication,” *Opt. Exp.*, vol. 26, no. 20, pp. 26355–26364, 2018.

[9] B. Janjua *et al.*, “Going beyond 4 Gbps data rate by employing RGB laser diodes for visible light communication,” *Opt. Exp.*, vol. 23, no. 14, pp. 18746–18753, 2015.

[10] J. R. D. Retamal *et al.*, “4-Gbit/s visible light communication link based on 16-QAM OFDM transmission over remote phosphor-film converted white light by using blue laser diode,” *Opt. Exp.*, vol. 23, no. 26, pp. 33656–33666, 2015.

[11] M. B. Rahaim, A. M. Vegni, and T. D. C. Little, “A hybrid radio frequency and broadcast visible light communication system,” in *Proc. IEEE GLOBECOM Workshop Opt. Wireless Commun.* IEEE, 2011, pp. 792–796.

[12] D. O’Brien, “Cooperation in optical wireless communications,” in *Cognitive Wireless Networks*. Berlin, Germany: Springer, 2007, pp. 623–634.

[13] M. S. Uddin, M. Z. Chowdhury, and J. Y. Min, “Priority-based resource allocation scheme for visible light communication,” in *Proc. IEEE 2nd Int. Conf. Ubiquition Future Netw.* 2010, pp. 247–250.

[14] J. R. Barry, J. M. Kahn, W. J. Krause, E. A. Lee, and D. G. Messerschmitt, “Simulation of multipath impulse response for indoor wireless optical channels,” *IEEE J. Sel. Areas Commun.*, vol. 11, no. 3, pp. 367–379, Apr. 1993.

[15] C. Chen, D. A. Basnayaka, X. Wu, and H. Haas, “Efficient analytical calculation of non-line-of-sight channel impulse response in visible light communications,” *IEEE J. Lightw. Technol.*, vol. 36, no. 9, pp. 1666–1682, May 2018.

[16] Z. Zhang, T. Zhang, J. Zhou, Y. Lu, and Y. Qiao, “Mobile phone camera based visible light communication using non-line-of sight(NLOS) link,” in *Proc. IEEE Int. Conf. Netw. Infrastructure Digit. Content*, 2018, pp. 35–39.

[17] W. Liu and Z. Xu, “Predicted and experimental performance of a long distance non-line of sight image sensor communication system,” in *Proc. IEEE Int. Conf. Commun. Workshops*, 2018, pp. 1–5.

[18] N. A. Mohammed and K. A. Badawi, “Design and performance evaluation for a non-line of sight VLC dimmable system based on SC-LPPM,” *IEEE Access*, vol. 6, pp. 52393–52405, 2018.

[19] S. Li, C. Gong, and Z. Xu, “Visible light communication performance in weak illumination environment,” in *Proc. IEEE Opto-Electron. Commun. Conf.*, 2015, pp. 1–3.

[20] X. Liu, C. Gong, S. Li, and Z. Xu, “Signal characterization and receiver design for visible light communication under weak illuminance,” *IEEE Commun. Lett.*, vol. 20, no. 7, pp. 1349–1352, Jul. 2016.

[21] T. Komine and M. Nakagawa, “Fundamental analysis for visible light communication system using LED lights,” *IEEE Trans. Consum. Electron.*, vol. 50, no. 1, pp. 100–107, Feb. 2004.

[22] N. Noels, H. Steendam, and M. Moeneclaey, “Carrier and clock recovery in (turbo) coded systems Cramer-Rao bound and synchronizer performance,” *J. Appl. Signal Process.*, vol. 2005, no. 6, pp. 972–980, 2003.